SUPPORTING INFORMATION

Anomalous Superionic Conductivity in van der Waals Lithium Thiophosphates Triggered by Interlayer Molecules

Jianing Liang, Yu Wu, Zongdong Sun, Cheng Zeng, Youwen Liu, Yinghe Zhao, Tianyou Zhai, and Huiqiao Li*

State Key Laboratory of Materials Processing and Die and Mould Technology, School of Materials Science and Engineering, Huazhong University of Science and Technology, Wuhan, Hubei 430074, China
*Corresponding Authors. Email: hqli@hust.edu.cn

Experimental section

Solid-state synthesis of LiInP$_2$S$_6$ The LiInP$_2$S$_6$ crystals have been synthesized by solid-state method. Owing to the air- and moisture-sensitivity of Li$_2$S, we manipulated all of the reagents and products in an Ar-filled glovebox. In brief, Li$_2$S (99.5%, Alfa Aesar), In (99.98%, Alfa Aesar), P$_2$S$_5$ (99%, Macklin), S (99.99%, Aladdin) were firstly ground and loaded into a graphite crucible at a molar ratio of 1:2:1:1 with mixed total mass of 2.0 g. The crucible was placed in a quartz tube, and subsequently the tube was flame-sealed under vacuum (<10^{-2} Pa). The sealed sample was heated slowly to 750 °C over at 10 h and dwelled for 72 h before cooling slowly at 6 h to 350 °C. The resultant samples were then removed from the crucible, ground, pelletized, and the whole process of flame-sealing and temperature treatment were repeated again. The resultant product of LiInP$_2$S$_6$ was a slightly pale-yellow crystalline powder.

Materials characterizations The X-ray Diffraction (XRD) patterns were obtained at room temperature on a Bruker AXS D2 Advance with a Cu Kα radiation (λ = 1.54178 Å). The morphology and thickness of nanoflake were characterized by optical microscope (BX51, OLMPUS) and atomic force microscope (AFM, Dimension Icon, Bruker). Raman spectra were carried out on WITec Alpha 300RS+ laser confocal Raman spectrometer equipped with an excitation wavelength 633 nm. The infrared (IR) spectra were recorded using a Thermo Scientific Nicolet iS50R in the range of 4000-400 cm^{-1}. Finely powdered samples were pressed into pellets with KBr. Solid-state nuclear magnetic resonance spectra (ss-NMR) were acquired using a Bruker avance III 500MHz NMR spectrometer. The spinning rate was 10 kHz and the spectra were referenced to an external LiCl standard at 0 ppm. Scanning electron microscope (SEM, FEI Quanta 650) equipped with EDS (energy-dispersive X-ray spectroscopy) was used to identify the morphology and element. Thermogravimetric analysis (TGA) and differential thermal analysis (DTA) were performed on PerkinElmer Diamond TG/DTA which were carried out in nitrogen atmosphere with heating and cooling rates of 10 °C·min^{-1}.

Conductivity measurement

Ionic conductivity: The ionic conductivities of LiInP$_2$S$_6$ series were determined by potentiostatic electrochemical impedance spectroscopy (PEIS) using by electrochemical workstation (Solartron analytical 1260+1287). The finely ground powders (>300 mesh) were placed between two 10 mm stainless steel dies, and the applied pressure was 480 MPa with about 0.6 mm resulting thickness of compressed samples. The pellet was quickly placed between two ion-blocking electrodes, which was orientated in a symmetric configuration. The pellets have a density of over 90% of the reported bulk materials (Table S1). The EIS spectra were collected using a sinusoidal voltage amplitude of 50 mV in a frequency range of 1 MHz to 10 Hz at the operating stack pressure of 370 MPa.[1] To determine the activation energy of the Li$^+$ conduction, the various temperature EIS measurements were conducted by using a climate chamber (E300, Zhongya Co., LTD) for about one hour or until the temperature fully

stabilized. The data were fit to an equivalent circuit using ZView software. The conductivities were calculated by using the equation: $\sigma_i = L/RS$. Where σ_i (S cm^{-1}) is conductivity, L (cm) is the thickness of pellet, R (ohms) is the resistance fitting from Nyquist plots, and S (cm^2) is the contact area between pellet and ion blocking electrode.

Electronic and protonic conductivity: The stainless steel as ion blocking electrode was used to obtain the ionic conductivity with applied DC polarization of 500 mV.[2] The PdH$_x$ electrode attached to the two sides of pellets and were used as protonic reversible electrodes to obtain the proton conduction with applied DC polarization of 500 mV.[3, 4]

Electrochemical characterization: In order to avoid the influence of the surface water, the hydrated LiInP$_2$S$_6$ powders were dried under vacuum at 80 ^{o}C. The Li metal symmetric cells assembly was carried out entirely in an argon-filled glove box and the LiInP$_2$S$_6$ powders was cold-pressed into a pellet as solid electrolyte. The EIS plots was measured on the Li/LiInP$_2$S$_6$/Li symmetric cells within a frequency range of 1 MHz to 1 Hz and sinusoidal voltage amplitude of 10 mV at room temperature.

Theoretical methods

Density functional theory (DFT) calculations: The ab initio computations have been carried out using the Vienna Ab-initio Simulation Package (VASP).[5] The band structure calculations and geometry optimization runs were performed using the projector-augmented wave (PAW) method, with Perdew-Burke-Ernzerhof (PBE) functional for generalized gradient approximation (GGA) exchange-correlation functional parameters.[6] The symmetry-unconstrained lattice parameters and atom coordinates were relaxed to the local total energy minimum, starting from the structure that we measured experimentally. Furthermore, for hydrated LiInP$_2$S$_6$, the anhydrous LiInP$_2$S$_6$ crystal data has been used as the initial model. For each case, the reciprocal space integrals have been evaluated using a kinetic-energy cut off of 520 eV for wave function on a 4×4×2 k-point grid generated uniformly by the Monkhorst−Pack method. The convergence threshold for geometry optimization has been set to 0.02 eV/Å. All structures were fully optimized by allowing for the volume, cell shape and atomic positions to change during the process. The projector augmented wave method was employed to describe the interactions between the core and valence electrons. To explore the charge transfer between different parts in the hybrid system, the Bader analysis method was adopted in the present work.

Bond valence site energy (BVSE) calculations: BVSE calculations were based on an ordering structure with minimal electrostatic energy and performed with the *SoftBV* program, using the single crystal structural model as input for analyzing automated ionic migration pathway.[7, 8] In this approach, Li$^+$ site energies are calculated for a dense grid of points with a resolution of 0.1 Å covering the crystal structure using the transferable Morse-type *SoftBV* force field. BVSE calculations have been used to study a wide variety of ion conductors and show good agreement with experimental and computational investigations. VESTA was used to produce crystal structure figures.[9]
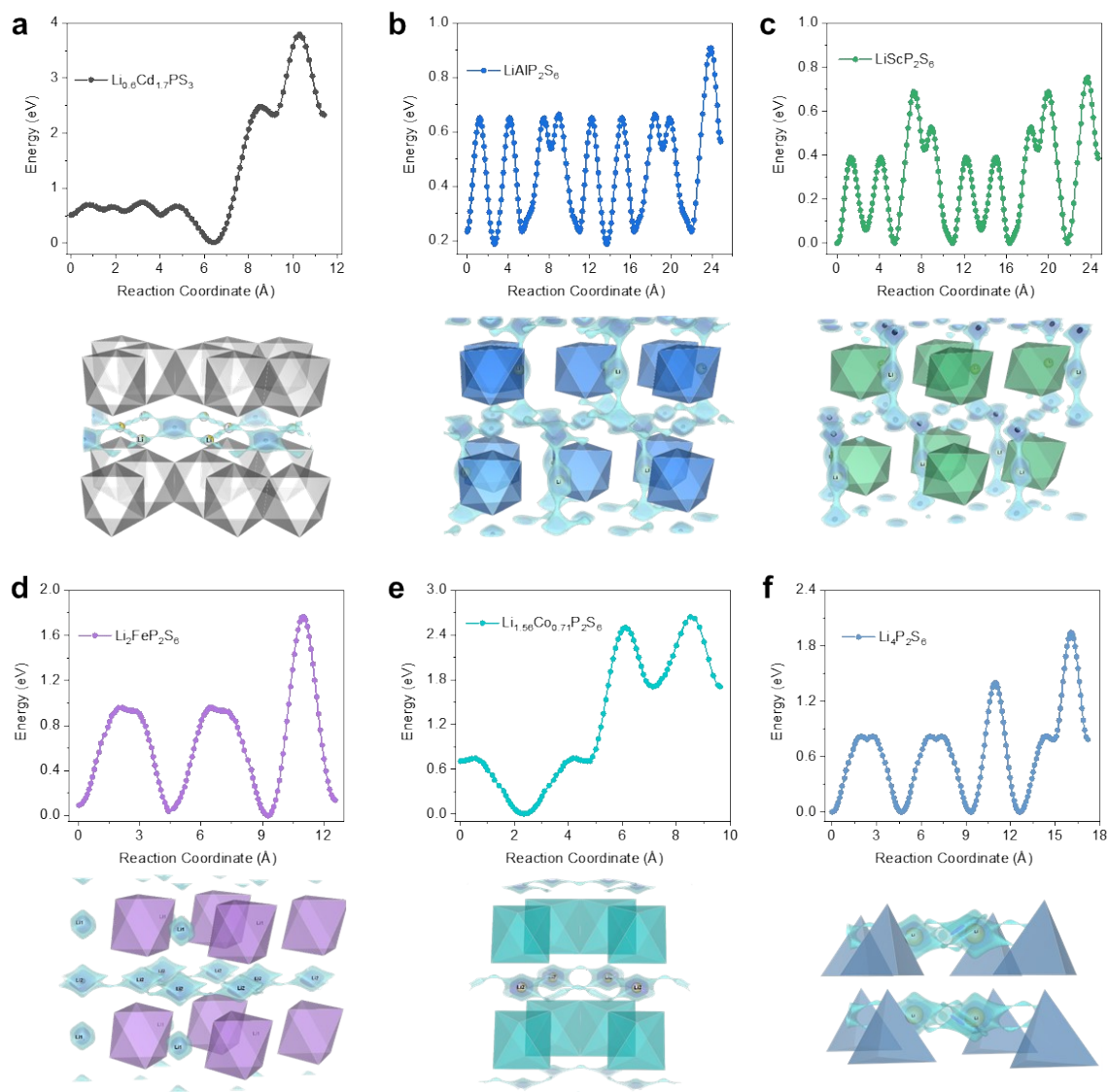
Supplementary results

Fig. S1 Li-ion migration pathways and energy landscapes in LTP conductors of (**a**) $Li_{0.6}Cd_{1.7}P_2S_6$; (**b**) $LiAlP_2S_6$; (**c**) $LiScP_2S_6$; (**d**) $Li_2FeP_2S_6$; (**e**) $Li_{1.56}Co_{0.71}P_2S_6$; and (**f**) $Li_4P_2S_6$.
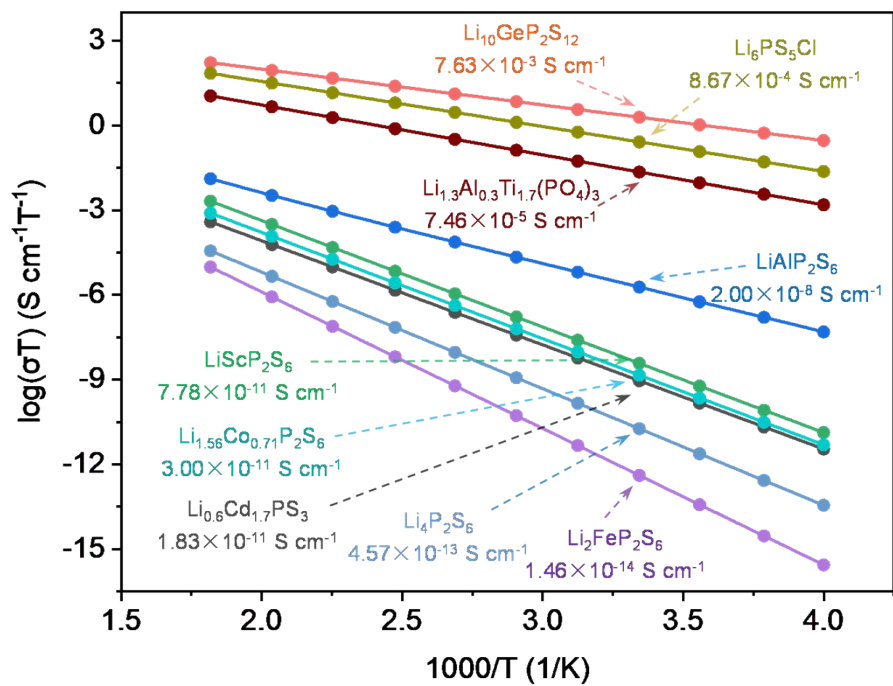
4

Fig. S2 Temperature dependence of ion conductivity of classical superionic conductors and several lithium thiophosphates.
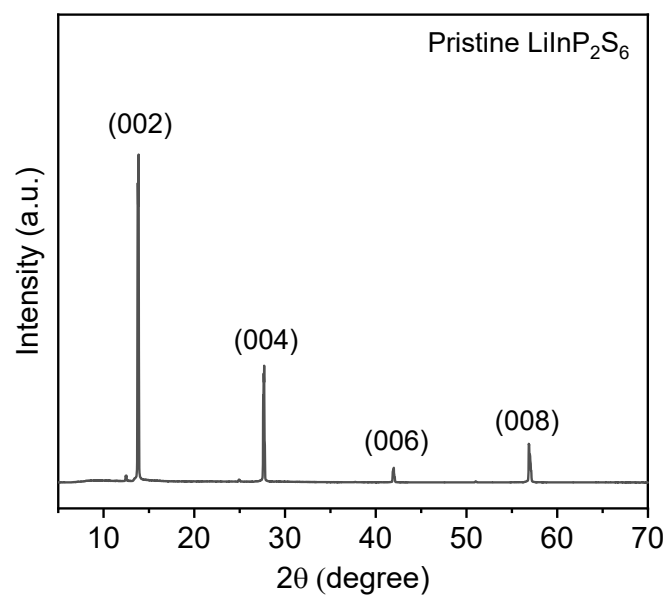
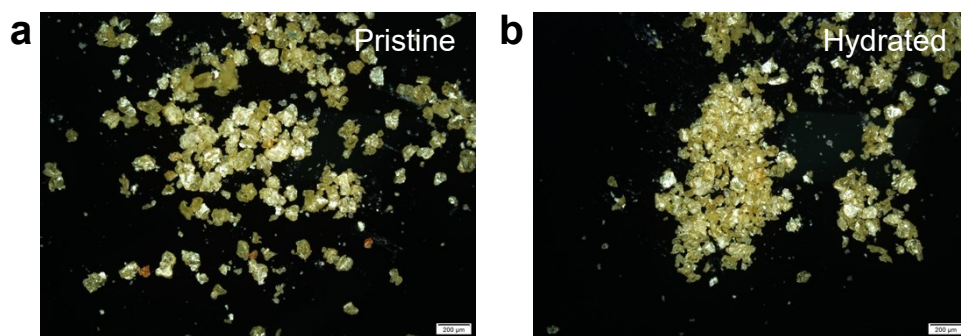**Fig. S3** Powder XRD pattern of pristine $LiInP_2S_6$ crystal with periodic diffraction peaks.

Fig. S4 Optical images of (**a**) pristine LiInP$_2$S$_6$ and (**b**) hydrated LiInP$_2$S$_6$ powder (> 300 mesh).
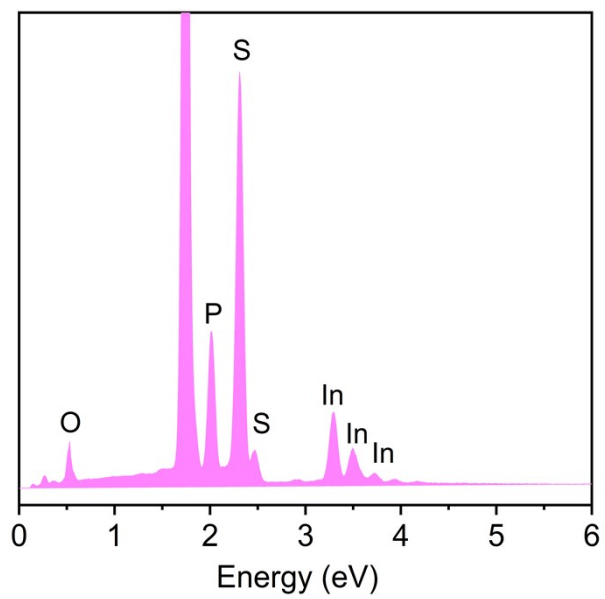
Fig. S5 EDS spectrum of hydrated $LiInP_2S_6$.
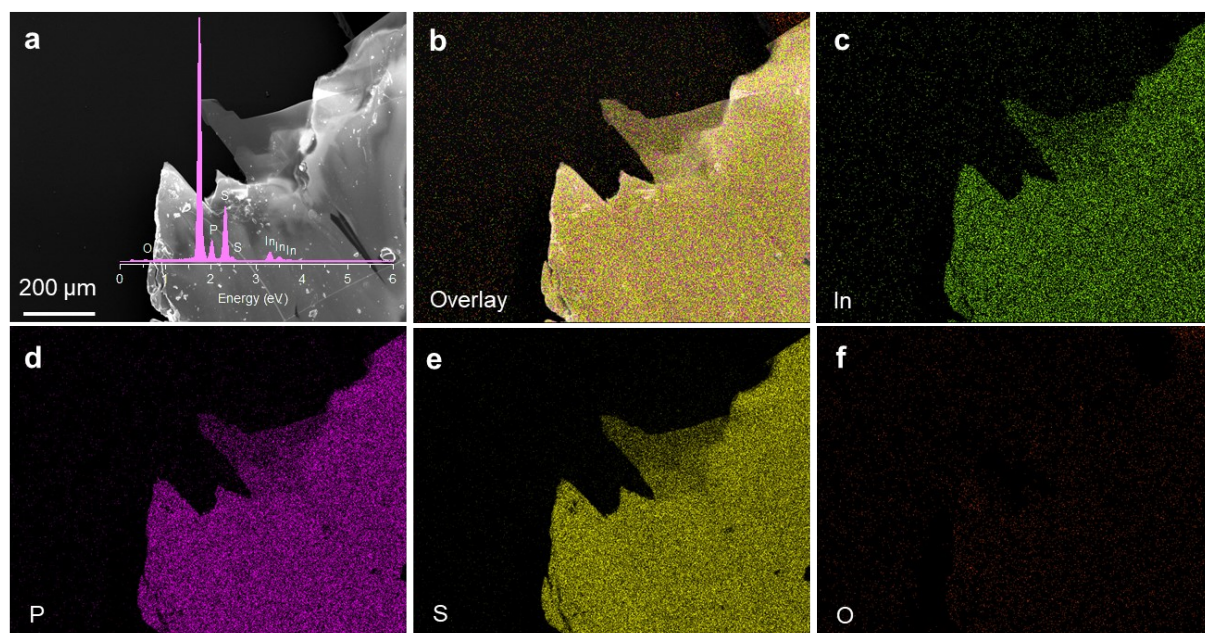
Fig. S6 Element mapping of pristine $LiInP_2S_6$. Inset in (**a**) is EDS spectrum.
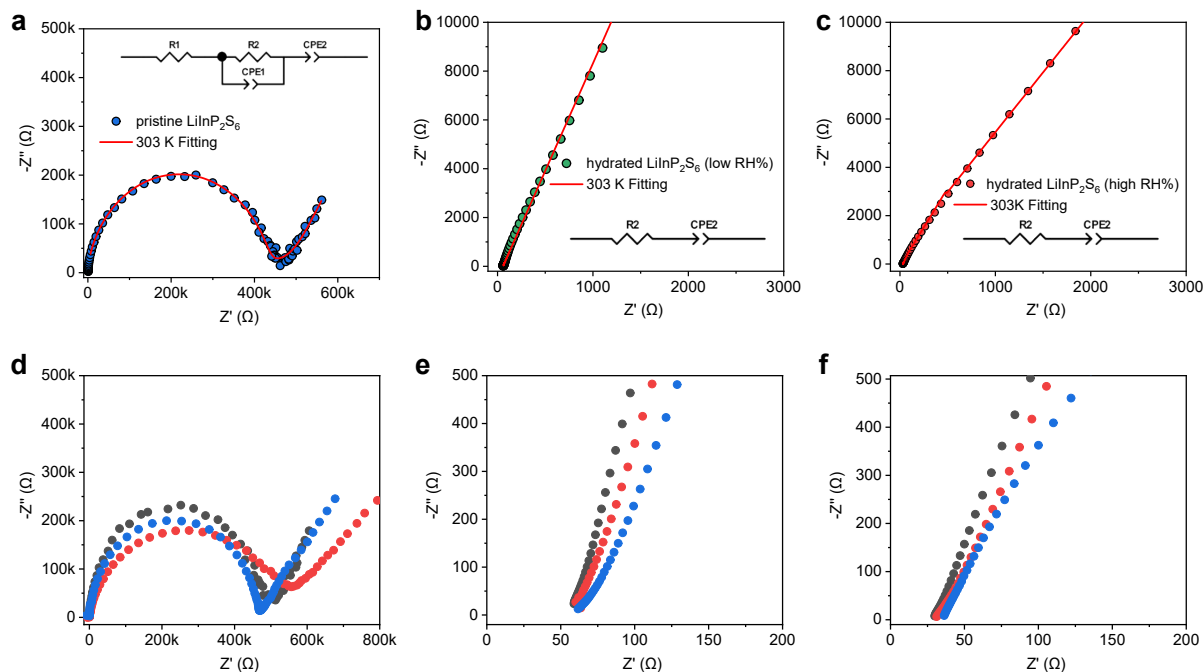
Fig. S7 Nyquist plot of impedance and fitting curves multiple measurement results of (**a**, **d**) pristine LinP$_2$S$_6$, (**b**, **e**) hydrated LiInP$_2$S$_6$ at low RH% (**c**, **f**) hydrated LiInP$_2$S$_6$ at high RH%. The inset shows the equivalent circuit used to analyze the impedance data. Where R1 represents bulk ion transport resistance. R2 and CPE1 correspond to the boundary ion transport resistance and the dielectric capacitance between the pellet and electrode, respectively. CPE2 is the dielectric capacitance between the pellet and electrode. The high-frequency semicircle is attributed to total ionic conduction.

Table S1 The parameters of different $LiInP_2S_6$ pellets.

Sample	Density (g cm^{-3})	Mass (mg)	Thickness (mm)	Density (%)
		146	0.670	92.3
$LiInP_2S_6$	3.008	147	0.686	90.7
		156	0.737	89.6
		94	0.575	89.7
$LiInP_2S_6 \cdot 3H_2O$	2.323	110	0.679	88.9
		102	0.614	91.1
		80	0.566	88.9
$LiInP_2S_6 \cdot 6H_2O$	2.026	85	0.596	89.7
		92	0.644	89.8
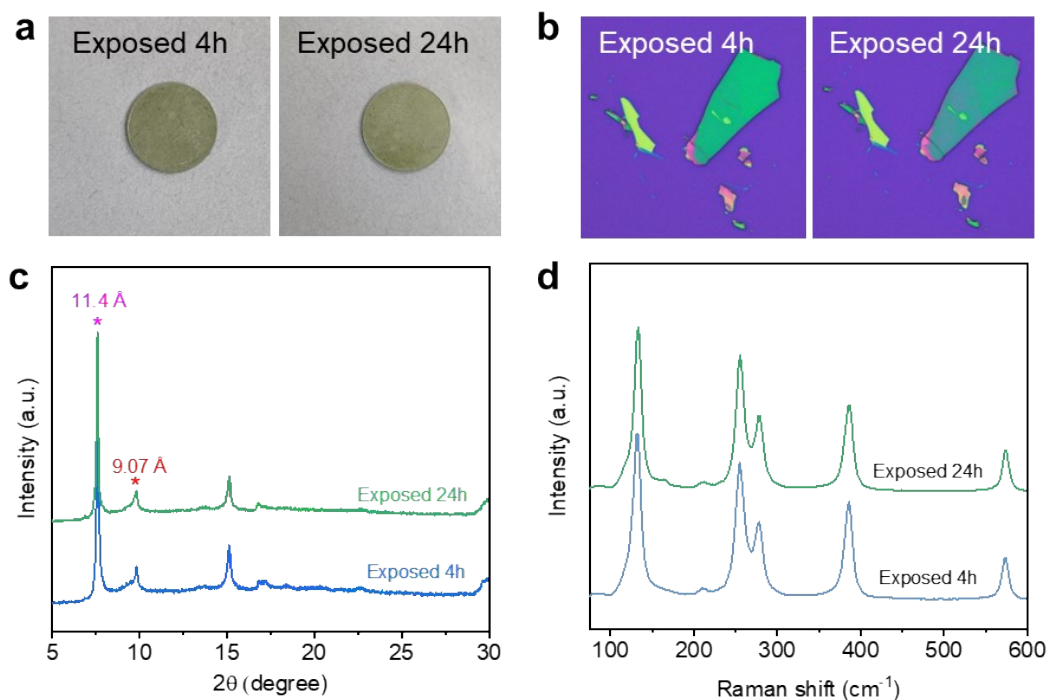
Fig. S8 Air stability of hydrated $LiInP_2S_6$ under different exposed times. Optics images of (**a**) pellet and (**b**) nanosheets; (**c**) XRD patterns and (**d**) Raman spectra of hydrated $LiInP_2S_6$ powder.

Notes: The surface characteristics of the hydrated $LiInP_2S_6$ material in air show that no deliquescence or decomposition occurs either on the pellet or on the more sensitive nanosheets when the exposed to ambient air over 24h. The XRD patterns and Raman spectra of hydrated $LiInP_2S_6$ powder also did not show any change.
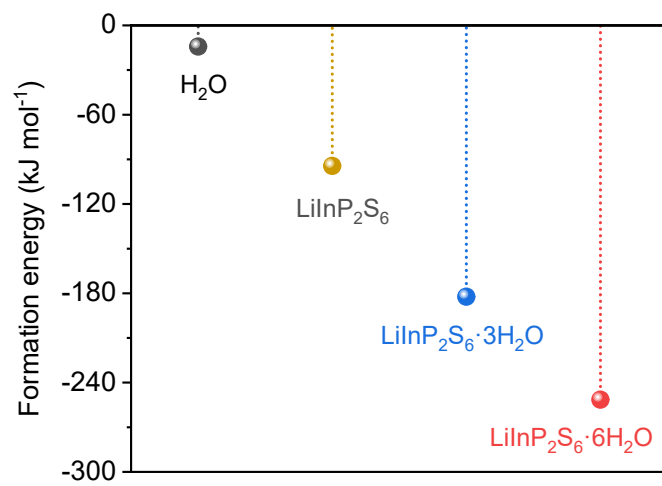
Fig. S9 The formation energy of H_2O, $LiInP_2S_6$, $LiInP_2S_6 \cdot 3H_2O$, and $LiInP_2S_6 \cdot 6H_2O$.
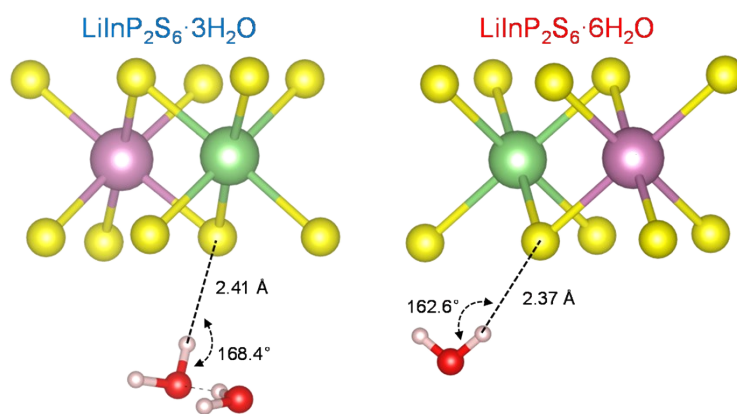
Fig. S10 The formation of hydrogen bond after harvested water molecules in the interlayer space of $LiInP_2S_6$.
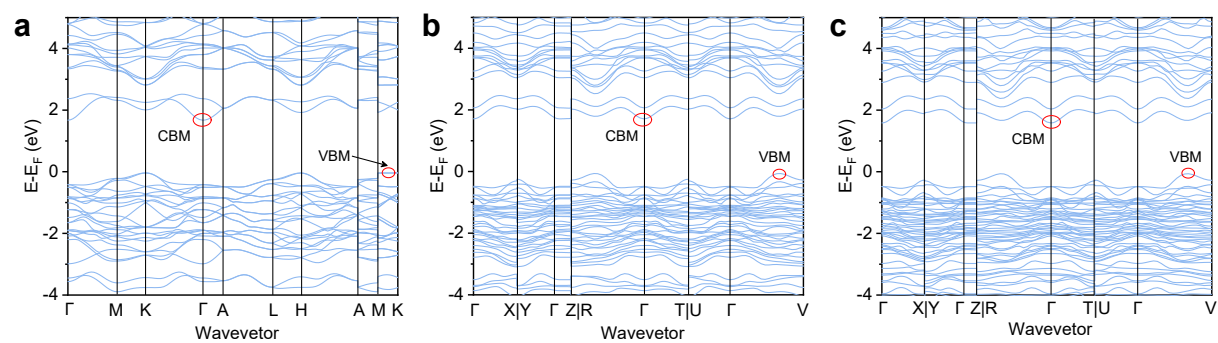
Fig. S11 Electronic band structure of (**a**) LinP$_2$S$_6$, (**b**) LiInP$_2$S$_6$·3H$_2$O, and (**c**) LiInP$_2$S$_6$·6H$_2$O. CBM, conduction band minimum; VBM, valence band maximum.
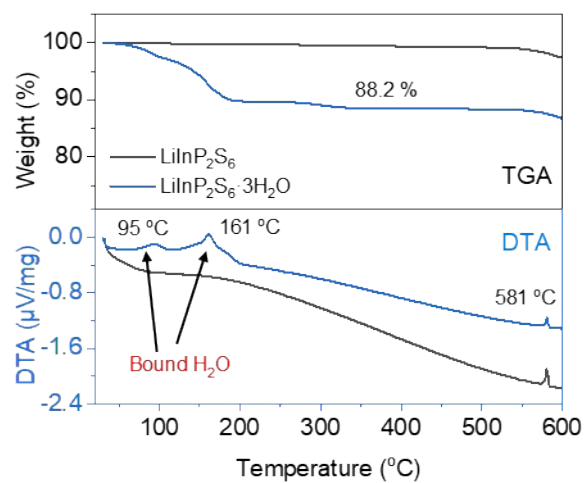
Fig. 12 Thermogravimetric and differential thermal analysis of the anhydrous and hydrated $LiInP_2S_6$ crystals.
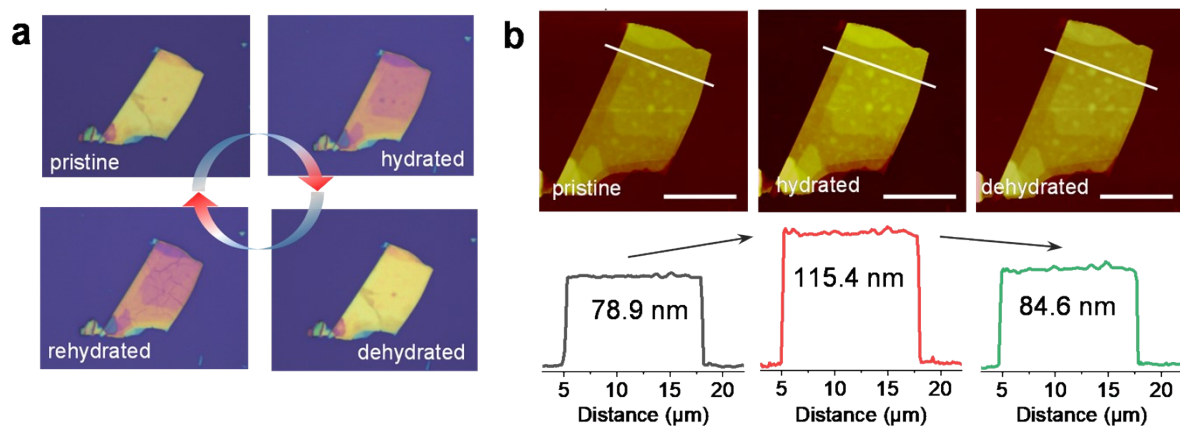
Fig. S13 (**a**) The reversible optical changes of LiInP$_2$S$_6$ nanoflake, (**b**) Structure evolution of AFM images, scale bar, 10 μm.
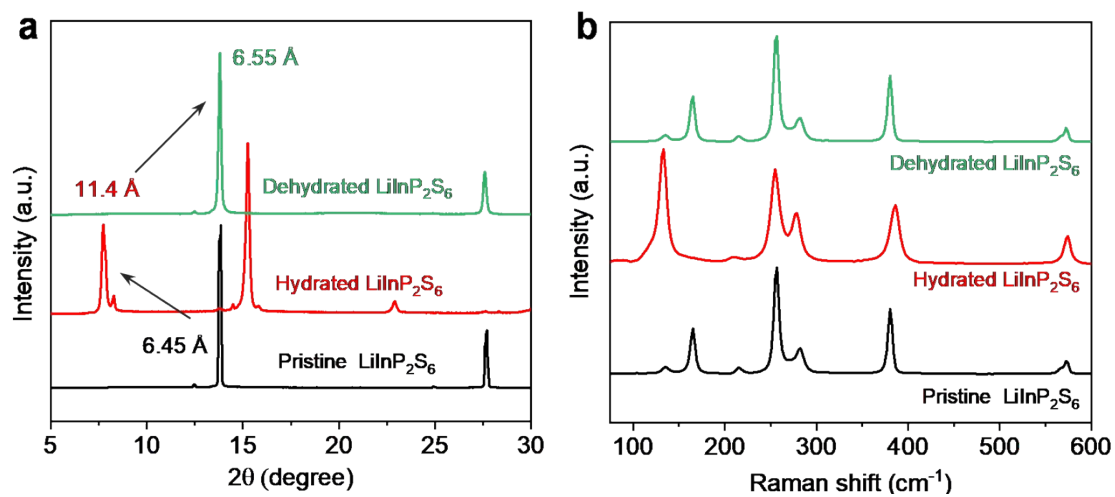
Fig. S14 (**a**) XRD patterns (**b**) Raman spectra of $LiInP_2S_6$ crystal at pristine, hydrated, and dehydrated states.
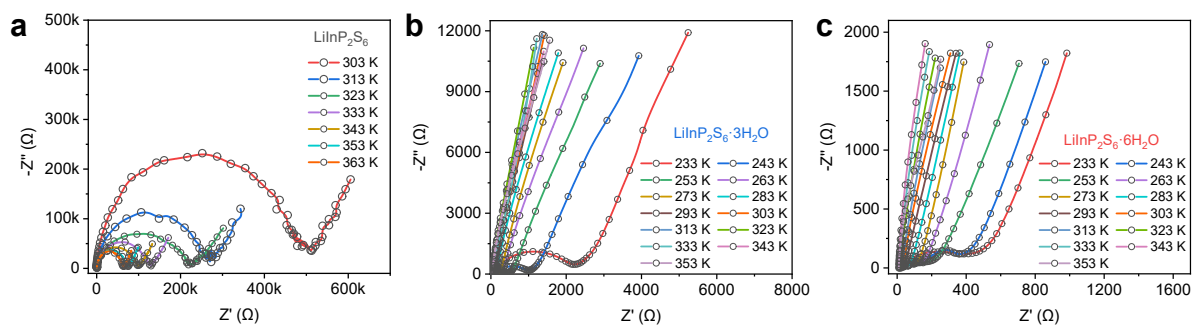
Fig. S15 Nyquist plots of impedance measured for (**a**) $LinP_2S_6$, (**b**) $LiInP_2S_6 \cdot 3H_2O$ and (**c**) $LiInP_2S_6 \cdot 6H_2O$ in the temperature range of 233−353 K.
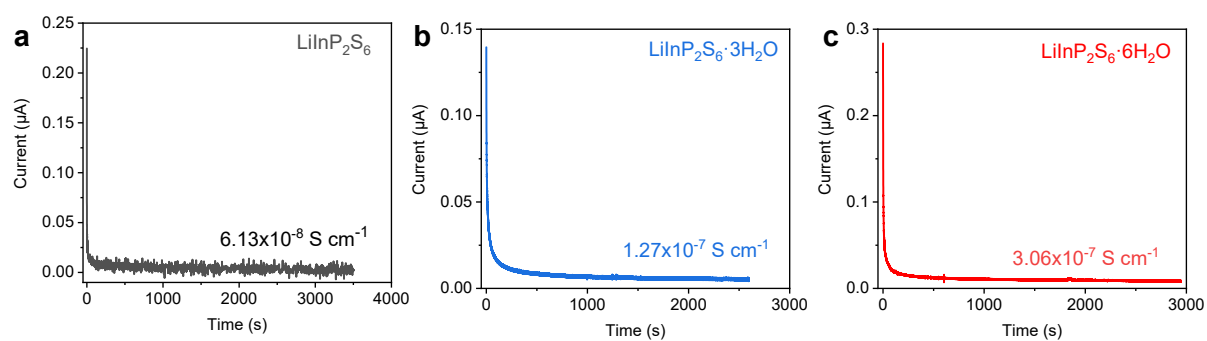
Fig. S16 Typical DC symmetric polarization curves (ion blocking electrodes) for (**a**) $LinP_2S_6$, (**b**) $LiInP_2S_6 \cdot 3H_2O$ and (**c**) $LiInP_2S_6 \cdot 6H_2O$ samples with voltage bias of 0.5 V for determining the electronic conduction contribution.
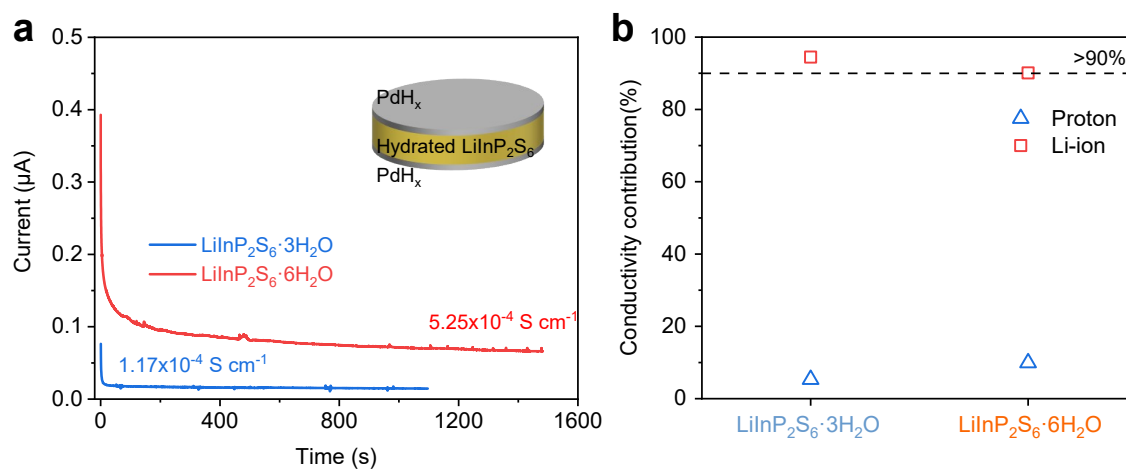
Fig. S17 (a) DC symmetric polarization curves (PdH$_x$ electrode) for hydrated LiInP$_2$S$_6$ sample with voltage bias of 0.5 V; (b) The conductivity contribution.
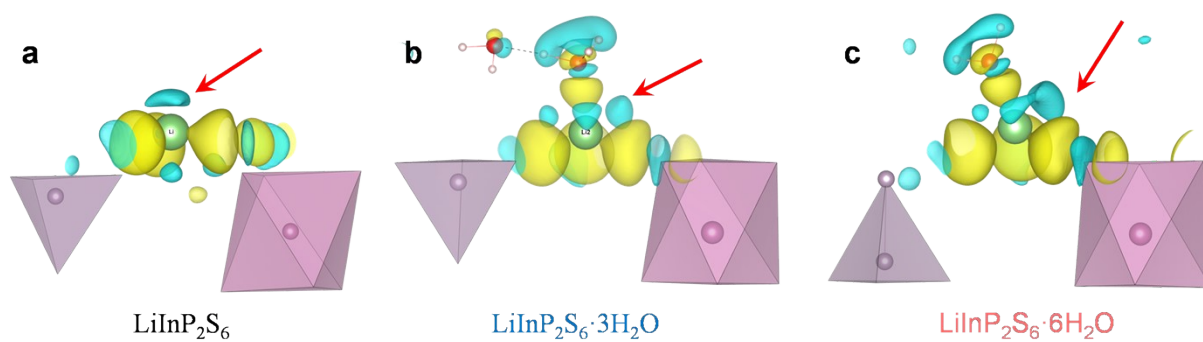
Fig. S18 Differential charge density of intermediate Li^+ in (**a**) $LiInP_2S_6$, (**b**) $LiInP_2S_6 \cdot 3H_2O$ and (**c**) $LiInP_2S_6 \cdot 3H_2O$. The yellow and cyan regions represent charge gaining and losing, respectively.
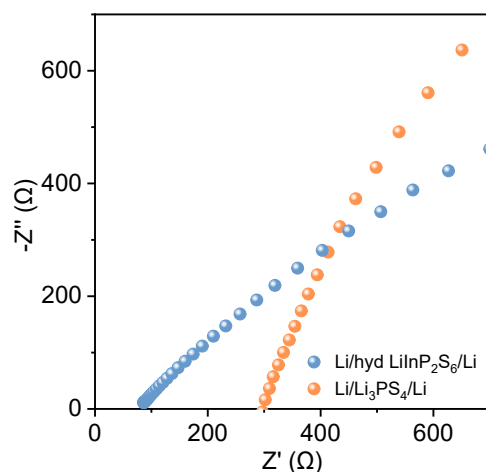
Fig. 19 The comparison of EIS plots in Li/hydrated LiInP$_2$S$_6$/Li and Li/ Li$_3$PS$_4$/Li symmetric cells.

References

1. J. M. Doux, Y. Yang, D. H. S. Tan, H. Nguyen, E. A. Wu, X. Wang, A. Banerjee and Y. S. Meng, *J. Mater. Chem. A*, 2020, **8**, 5049-5055.

2. H. Xiao, W. Linbin, H. Zhen, L. Jiu and X. Xiaoxiong, *Energy Stor. Sci. Tech.*, 2020, **9**, 477-500.

3. X. Qian, L. Chen, L. Yin, Z. Liu, S. Pei, F. Li, G. Hou, S. Chen, L. Song, K. H. Thebo, H. M. Cheng and W. Ren, *Science*, 2020, **370**, 596-600.

4. X. Yu and W. Ren, *Nat. Commun.*, 2023, **14**, 3998.

5. J. Hafner, *J. Comput. Chem.*, 2008, **29**, 2044-2078.

6. J. P. Perdew, K. Burke and M. Ernzerhof, *Phys. Rev. Lett.*, 1996, **77**, 3865.

7. L. L. Wong, K. C. Phuah, R. Dai, H. Chen, W. S. Chew and S. Adams, *Chem. Mater.*, 2021, **33**, 625-641.

8. H. Chen, L. L. Wong and S. Adams, *Acta Cryst.*, 2019, **B75**, 18-33.

9. K. Momma and F. Izumi, *J. Appl. Cryst.*, 2011, **44**, 1272-1276.